

**Observation of Photonic Topological Valley Hall Edge States**Jiho Noh,<sup>1</sup> Sheng Huang,<sup>2</sup> Kevin P. Chen,<sup>2</sup> and Mikael C. Rechtsman<sup>1</sup><sup>1</sup>*Department of Physics, The Pennsylvania State University, University Park, Pennsylvania 16802, USA*<sup>2</sup>*Department of Electrical and Computer Engineering, University of Pittsburgh, Pittsburgh, Pennsylvania 15261, USA*

(Received 31 May 2017; published 6 February 2018)

We experimentally demonstrate topological edge states arising from the valley-Hall effect in two-dimensional honeycomb photonic lattices with broken inversion symmetry. We break the inversion symmetry by detuning the refractive indices of the two honeycomb sublattices, giving rise to a boron nitridelike band structure. The edge states therefore exist along the domain walls between regions of opposite valley Chern numbers. We probe both the armchair and zigzag domain walls and show that the former become gapped for any detuning, whereas the latter remain ungapped until a cutoff is reached. The valley-Hall effect provides a new mechanism for the realization of time-reversal-invariant photonic topological insulators.

DOI: [10.1103/PhysRevLett.120.063902](https://doi.org/10.1103/PhysRevLett.120.063902)

Photonic topological insulators (PTIs) are dielectric structures that possess topologically protected edge states that are under certain circumstances robust to scattering by disorder [1–12]. There are two categories of PTIs: those that break time-reversal symmetry [3,7] and those that preserve it [8,9,11]. In PTIs that break time-reversal symmetry, there exist one-way edge states, which ensure their robustness, due to the lack of counterpropagating partners at the same frequency. In those that preserve it, there exist counterpropagating edge states that are protected only against certain classes of disorder. However, the latter can be more straightforward to realize, because they do not require strong time-reversal breaking. PTIs have been of interest due to the possibility of photonic devices that are less sensitive to fabrication disorder.

In the valley-Hall effect, broken inversion symmetry in a two-dimensional (2D) honeycomb lattice causes opposite Berry curvatures in the two valleys of the band structure [13,14] and has been realized in solid-state 2D materials [15–19]. The valley-Hall effect is time-reversal invariant and has common characteristics with the spin Hall effect [20], where the two valleys in the band structure are used as “pseudospin” degrees of freedom. It was shown theoretically that valley-Hall topological edge states would arise in analogous photonic structures [21–27]. In addition, valley-Hall topological edge states have also been recently studied in the context of topological valley transport of sound in sonic crystals [28].

Here, we present the experimental observation of photonic topological valley-Hall edge states at domain walls between valley-Hall PTIs of opposite valley Chern numbers. The bulk-edge correspondence ensures the presence of edge states: The change in the valley Chern number across the domain wall is associated with the existence of counterpropagating edge states [19,29,30]. We realize

photonic valley-Hall topological edge states in evanescently coupled waveguide arrays, i.e., photonic lattices, fabricated using the femtosecond direct laser-writing technique [31]. We probe different types of domain walls, namely, the armchair and zigzag edges. We also enter a fully gapped regime, which is not accessible in solid-state 2D materials. The topological protection associated with the valley-Hall effect applies as long as a single valley is populated and does not mix with the other valley. In general, disorder that has only low spatial frequency components (i.e., is sufficiently smooth) will not mix the valleys.

We begin by describing our experimental system, which is composed of an array of evanescently coupled waveguides arranged in a honeycomb lattice geometry. The laser-writing technique allows us to arbitrarily control the refractive index of the waveguides, by varying the average power of the pulse train in the femtosecond direct laser-writing procedure. The geometries of lattices having armchair and zigzag edges at their domain wall are depicted in Figs. 1(a) and 1(b), respectively (see Supplemental Material for microscope images [32]).

The interface is between two regions (top and bottom) that are both honeycomb lattices with opposite signs of the on-site energy detuning between the two component sublattices, which breaks inversion symmetry within each given lattice. Experimentally, the detuning is carried out by controlling the refractive index of the waveguide at each site. Figure 1(c) shows the 2D bulk band structure of the inversion-symmetry-broken honeycomb lattice, clearly showing the two valleys. This is simply an inversion-symmetry-broken variation of the photonic honeycomb lattices described in Refs. [33–35], and, as in the graphene band structure, two valleys are located at two nonequivalent  $K$  and  $K'$  points in the first Brillouin zone. The valley Chern

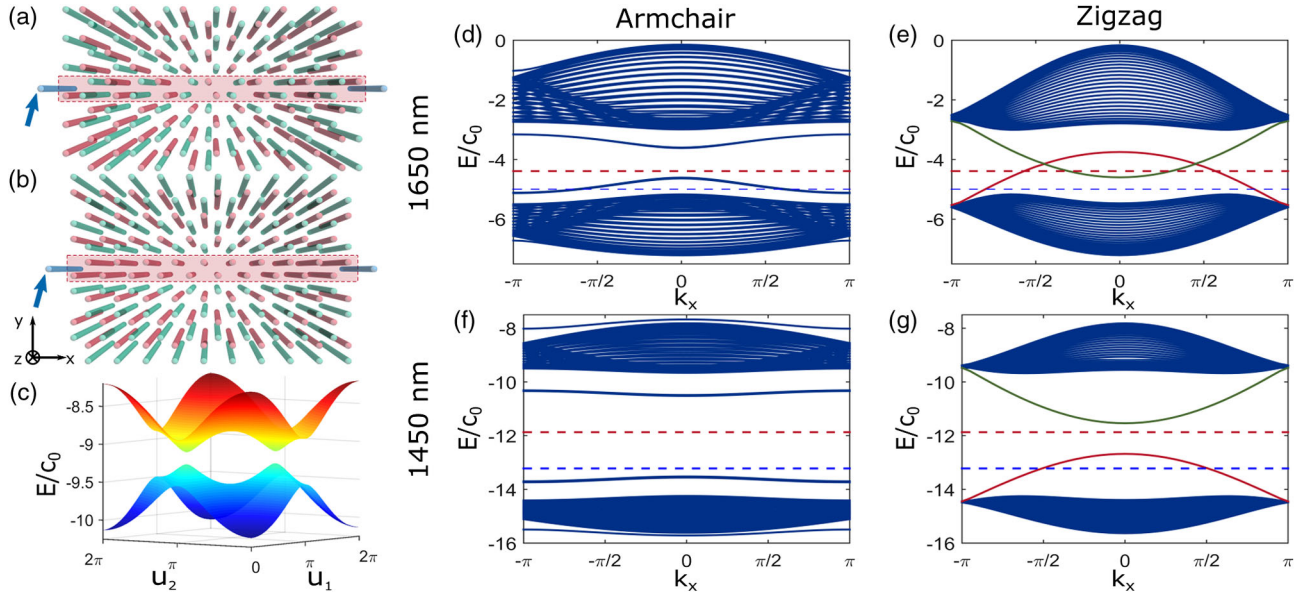


FIG. 1. (a) Schematic diagram of inversion-symmetry-broken honeycomb lattices with armchair and (b) and zigzag edge domain walls. Red and green waveguides indicate a different refractive index, and blue indicates straw waveguides. Red shaded regions indicate domain walls. (c) Band structure of the inversion-symmetry-broken graphene defined by  $u_1 \mathbf{b}_1 + u_2 \mathbf{b}_2$ , where  $\mathbf{b}_1 = (2\pi/3a)(1, \sqrt{3})$  and  $\mathbf{b}_2 = (2\pi/3a)(1, -\sqrt{3})$  are reciprocal lattice vectors and  $a$  is the lattice constant. (d) Continuum edge band structures with periodic boundary conditions on both the  $x$  and  $y$  directions at  $\lambda = 1650$  nm and  $k_y = 0$  when the armchair or (e) zigzag edges are placed at the domain wall. (f),(g) Corresponding band structures at  $\lambda = 1450$  nm. Red and blue dashed lines indicate energies of eigenmodes that are excited by coupling with the straw waveguide when we excited modes at midgap and significantly below midgap, respectively. Green and red bands in (e) and (g) indicate edge states located at the domain wall close to and far away from straw waveguides, respectively. Therefore, only the green bands are accessible in the experiment.

number is defined as the difference in the integrated Berry curvature associated with the two valleys. Since the Berry curvature points in the opposite directions ( $+z, -z$ ) in the two valleys in a given lattice, and the sign is given by that of the inversion-breaking term, it follows that the top and bottom lattices in Figs. 1(a) and 1(b) must have opposite valley Chern numbers and thus have valley-protected edge states.

The diffraction of light through the waveguide array is governed by the paraxial wave equation:

$$i\partial_z \psi(\mathbf{r}, z) = -\frac{1}{2k_0} \nabla_{\mathbf{r}}^2 \psi(\mathbf{r}, z) - \frac{k_0 \Delta n(\mathbf{r})}{n_0} \psi(\mathbf{r}, z) \equiv H_{\text{cont}} \psi(\mathbf{r}, z), \quad (1)$$

where  $\psi(\mathbf{r}, z)$  is the envelope function of the electric field  $\mathbf{E}(\mathbf{r}, z) = \psi(\mathbf{r}, z) \exp[i(k_0 z - \omega t)] \hat{x}$ ,  $k_0 = 2\pi n_0 / \lambda$  is the wave number within the medium,  $\lambda$  is the wavelength of the laser,  $\omega = 2\pi c / \lambda$ ,  $n_0$  is the refractive index of the ambient glass, and  $\nabla_{\mathbf{r}}^2$  is the Laplacian in the transverse ( $x, y$ ) plane.  $H_{\text{cont}}$  is the continuum Hamiltonian for propagation of the wave in the photonic lattice.  $\Delta n$  is the refractive index of the waveguide relative to the index of our medium, which acts as an effective potential in the Schrödinger equation, Eq. (1). The inversion symmetry of the lattice is broken by having different  $\Delta n_A$  and  $\Delta n_B$  for

waveguides in sublattices  $A$  and  $B$ , respectively, which is analogous to having different on-site energies  $E_A$  and  $E_B$  in the condensed-matter context. Furthermore, we write two additional waveguides, which we call “straw waveguides” (as discussed previously in Ref. [36]) into which light is injected. The straws are weakly coupled to the lattice, allowing them to act as an external drive that is injecting light into the system without altering the system’s intrinsic modes. Furthermore, varying the refractive index of the straw,  $\Delta n_s$ , allows for the control of the propagation constant (i.e., energy) of the modes being injected into the structure. By analogy with condensed-matter systems, the straw allows us to control the effective “Fermi energy” of the system, allowing coupling only to modes of a given energy  $E$ .

The emergence of valley-Hall topological edge states is shown in a full-continuum calculation by diagonalizing  $H_{\text{cont}}$  in Eq. (1) of 2D inversion-symmetry-broken honeycomb lattice ribbons [as shown in Figs. 1(d)–(g)]. The unit cell is a strip that is periodic in the horizontal direction (with a periodicity given by the lattice constant) but is many unit cells in the vertical direction and includes the domain wall (in fact, it must contain a minimum of two domain walls). The eigenvalues of the Schrödinger operator given in Eq. (1) are the energies of the calculated eigenmodes. Band structures and therefore band gap sizes can be engineered by sweeping across  $\Delta E / c_0$ , where  $\Delta E = E_A - E_B$  and  $c_0$  is the

coupling strength between the nearest-neighbor waveguides. Experimentally,  $\Delta E$  can be controlled by varying both  $\Delta n_A$  and  $\Delta n_B$ , and  $c_0$  can be increased by decreasing the distance between the nearest-neighbor waveguides,  $d$ , and increasing  $\lambda$ ; calculated  $c_0(\lambda)$  at fixed  $d = 19 \mu\text{m}$  for  $\lambda = 1650 \text{ nm}$  and  $\lambda = 1450 \text{ nm}$  are  $2.69$  and  $1.76 \text{ cm}^{-1}$ , respectively (for the remainder of the work, we logically order long wavelength before short wavelength, because the band gap increases with a decreasing wavelength). The initial calibration of  $c_0(\lambda)$  is obtained by measuring beating in two coupled waveguides as a function of the wavelength and distance [37]. Figures 1(d) and 1(e) show band structures when armchair and zigzag edges are placed at the domain wall, respectively, where  $\lambda = 1650 \text{ nm}$ ,  $d = 19 \mu\text{m}$ ,  $\Delta n_A = 2.50 \times 10^{-3}$ , and  $\Delta n_B = 2.90 \times 10^{-3}$ , and Figs. 1(f) and 1(g) show corresponding band structures with the same  $d$ ,  $\Delta n_A$ , and  $\Delta n_B$  but with  $\lambda = 1450 \text{ nm}$ . For both structures with armchair and zigzag edge domain walls, the bulk band gap opens immediately as  $\Delta E/c_0$  becomes nonzero. However, the behaviors of the edge states are different for each case: For the structure with the armchair domain wall, the edge band gap opens immediately after  $\Delta E/c_0$  becomes nonzero [Figs. 1(d) and 1(f)]. For the structure with the zigzag domain wall, there exist edge states at midgap for small  $\Delta E/c_0$  [Fig. 1(e)], which indicates the edge band gap would open only at finite  $\Delta E/c_0$  [Fig. 1(g)]. The two edge state bands shown in green and red in Figs. 1(e) and 1(g) are localized next to the straw waveguides (in the center of the figure) and on the opposite termination (assuming periodic boundary conditions), respectively. Therefore, only the green bands will be physically accessible in the experiment. This difference between the armchair and zigzag edges arises because the orientation of the armchair termination is such that it mixes the two valleys; since they may scatter between them, this allows for a matrix element for a gap to open even for small  $\Delta E/c_0$ . However, the zigzag edge runs parallel to the line that connects the two valleys in  $k$ -space, implying that the presence of the edge does not connect them, allowing them to remain ungapped.

To experimentally observe the emergence of topological edge states, a beam was launched at the input facet of the sample through a lens-tipped fiber, which allows coupling into a selected straw waveguide. The length of the sample is  $7 \text{ cm}$  and the radii of the major and minor axes of the waveguides are  $4.9$  and  $3.2 \mu\text{m}$ , respectively. Here, the refractive index of the straw waveguides was calibrated to inject light at midgap and significantly below midgap, in different devices. The energies of the straw waveguide modes were calculated by diagonalizing  $H_{\text{cont}}$  of a single waveguide. In Fig. 2, we present the observed diffracted light at the output facet of the array for the case of midgap driving [red dashed lines in Figs. 1(d)–1(g)]. Here, the calculated energy of the straw waveguide modes at the midgap energy were  $-4.39c_0$  and  $-11.87c_0$  for  $1650$  and  $1450 \text{ nm}$ , respectively. We plot the edge intensity ratio,

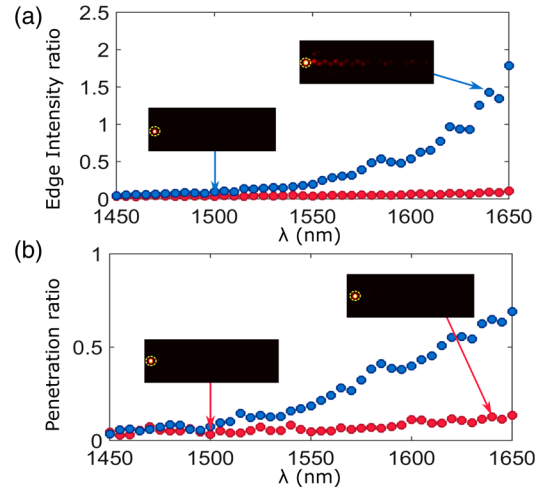


FIG. 2. (a) Measured edge intensity ratio and (b) penetration ratio when we excite modes at midgap. Blue and red dots are measured at zigzag and armchair edge domain walls, respectively. (Inset) Diffracted light measured at the output facet. Waveguides where light is injected are marked with a yellow dashed circle.

which is the ratio of the light intensity along the domain wall ( $I_{\text{edge}}$ ) to the light intensity in the straw, and the penetration ratio, which is ratio of the intensity of light that penetrates into the structure to the total light intensity ( $I$ ). First, in the photonic lattice with the armchair domain wall, we observe that most of the light coupled into the straw waveguide stayed in the straw, not coupling into the waveguide array (Fig. 2; see Supplemental Material [32], Movie 1). Both the measured edge intensity ratio and the penetration ratio were relatively very small, which indicates the presence of the band gap between the edge modes; i.e., no edge states are available to transport light through the array. This experimental result agrees with the full-continuum calculation having red dashed lines not crossing any edge states in the band structure as shown in Figs. 1(d) and 1(f). On the other hand, from the analogous structure with the zigzag domain wall, we observed a clear excitation of edge states along the domain wall, which becomes more significant as the wavelength is increased (Fig. 2; see Supplemental Material [32], Movie 2). This indicates that, at  $\lambda = 1450 \text{ nm}$ , the band gap is fully open so that the straw waveguide mode is not able to couple into the domain wall; but as we increase  $\lambda$  to make  $\Delta E/c_0$  subsequently decrease, the band gap becomes smaller and eventually edge states couple with the straw waveguide mode at midgap. Furthermore, the sharp increase in the edge intensity ratio and the penetration ratio indicates that there exist edge states having midgap energy. This experimentally establishes the presence of valley-Hall edge states at midgap for the zigzag edge, and the lack thereof for the armchair edge, consistent with theoretical predictions described above.

We further probe the valley-Hall edge states by changing  $\Delta n_s$  of the straw waveguides, while keeping  $\Delta n_A$  and  $\Delta n_B$  the same, such that we excite modes at a different energy

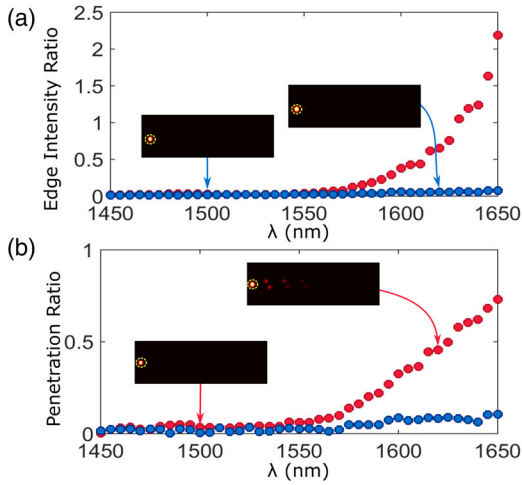


FIG. 3. (a) Measured edge intensity ratio and (b) penetration ratio when we excited modes significantly below midgap. Blue and red dots are measured at zigzag and armchair edge domain walls, respectively. (Inset) Diffracted light measured at the output facet. Waveguides where light is injected are marked with a yellow dashed circle.

[blue dashed lines in Figs. 1(d)–1(g)]. Here, the calculated energies of the straw waveguide modes were  $-4.98c_0$  and  $-13.22c_0$  for 1650 and 1450 nm, respectively. For the armchair edge, the energy coincides with edge bands at  $\lambda = 1650$  nm but not at  $\lambda = 1450$  nm [Figs. 1(d) and 1(f)]. Therefore, we observe confinement to the input straw waveguide at  $\lambda = 1450$  nm followed by increased penetration along the domain wall with an increasing wavelength and strong penetration by  $\lambda = 1650$  nm (Fig. 3; see Supplemental Material [32], Movie 3). For the zigzag edge, however, the energy does not coincide with the state along the domain wall boundary [Fig. 1(b)], whose dispersion is shown in green in Figs. 1(e) and 1(g), but rather the confined state that arises on the opposite side of the system when periodic boundary conditions are imposed in the vertical direction, shown in red in Figs. 1(e) and 1(g). In other words, since the only edge states localized near the straw waveguide are those drawn in green, there is no penetration along the zigzag edge for this energy. Therefore, no penetration is observed in the entire wavelength range for the zigzag edge (Fig. 3; see Supplemental Material [32], Movie 4).

In order to confirm that the small edge intensity ratio and penetration ratio measured at  $\lambda = 1450$  nm are indeed the consequence of a large edge state band gap, as opposed to simply weak interwaveguide coupling, we injected light at the center of the domain wall such that edge states are directly excited [Figs. 4(a) and 4(b)]—in other words, we did not attempt to fix the energy by using the straw. If the small penetration ratios were the result of weak coupling strength between the nearest-neighbor waveguides, the injected light would be expected to be strongly confined at the center of the waveguide array, where it is initially

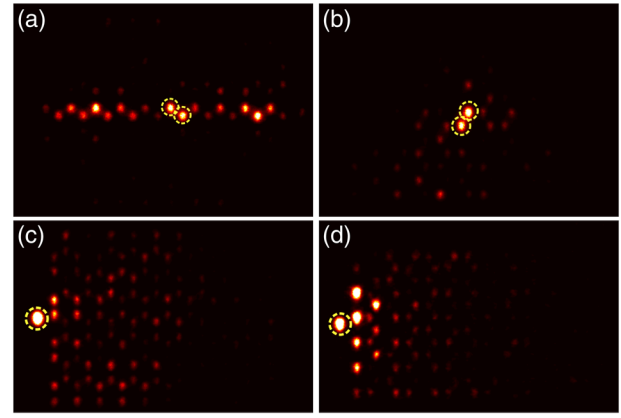


FIG. 4. (a) Diffracted light measured at the output facet when we inject directly at the center of the zigzag and (b) the armchair domain walls. (c) Diffracted light measured at the output facet when  $\Delta n_A = \Delta n_B = \Delta n_s$  and the straw waveguide mode is initially excited for the zigzag orientation and (d) the armchair domain walls. All measurements are carried out at  $\lambda = 1450$  nm. Waveguides where light is injected are marked with a yellow dashed circle.

injected. However, for both waveguide arrays with zigzag and armchair domain walls, we observed light diffracting along the domain wall and into the bulk. There is significantly more diffraction along the zigzag edge as compared to the armchair edge, because the armchair edge band is nearly flat and the zigzag edge band is highly dispersive [see Figs. 1(d)–1(g)]. However, in both cases, there is clear diffraction into the bulk of the structure, as is expected when we do not drive at a fixed energy using the straw. Furthermore, we examine the case where the system has no inversion breaking whatsoever, namely,  $\Delta n_A = \Delta n_B = \Delta n_s$ . In this case, there is no band gap and therefore no edge state along the domain wall of Fig. 1(a),(b). Upon injecting light into the straw waveguide, we observe diffraction into the bulk for both structures shown in Figs. 1(a) and 1(b) of the zigzag and armchair orientation [Figs. 4(c) and 4(d)]. Some excitation of the left edge of the structure is observed, corresponding to the bearded edge state of the honeycomb lattice. Taken together, these results show that the straw waveguide acts as a reliable tool for fixing the propagation constant for use in directly observing the presence in the valley-Hall edge states in the wavelength range 1450–1650 nm.

In summary, we have experimentally realized photonic valley-Hall topological edge states in 2D honeycomb photonic lattices with broken inversion symmetry. We have experimentally demonstrated that it is possible to open very large band gaps and therefore enter a fully gapped regime even for the structure with zigzag edge domain walls, which was not possible in solid-state 2D materials. Auxiliary straw waveguides placed at either end of the domain walls made it possible to excite a desired energy within the bulk band gap, allowing for a convenient tool for

setting the waveguide array energies. Being a time-reversal-invariant system, the valley-Hall effect could provide a straightforward route towards realizing photonic topological edge states, particularly in an on-chip platform. Thus, while valley-Hall edge states are not rigorously protected against any class of disorder, they will be protected against disorder that is sufficiently smooth (and thus does not allow intervalley scattering). The linear, static, and nonmagnetic nature of the design will also allow for lower optical loss compared to other approaches to topologically protected photonic states (for example, magnetic materials are typically lossy). Furthermore, the photonic valley-Hall effect could provide a natural platform for photonic quantum simulation of topological phenomena, perhaps by coupling the photonic modes to atoms or excitons.

M. C. R. acknowledges the National Science Foundation under Grant No. ECCS-1509546 and the Penn State MRSEC, Center for Nanoscale Science, under Grant No. NSF DMR-1420620 as well as the Alfred P. Sloan Foundation under Fellowship No. FG-2016-6418. K. C. acknowledges the National Science Foundation under Grants No. ECCS-1509199 and No. DMS-1620218.

J. N. and S. H. contributed equally to this work.

*Note added.*—Recently, we became aware of an analogous work in the microwave regime [38].

- 
- [1] L. Lu, J. D. Joannopoulos, and M. Soljačić, Topological photonics, *Nat. Photonics* **8**, 821 (2014).
- [2] F. D. M. Haldane and S. Raghu, Possible Realization of Directional Optical Waveguides in Photonic Crystals with Broken Time-Reversal Symmetry, *Phys. Rev. Lett.* **100**, 013904 (2008).
- [3] Z. Wang, Y. Chong, J. D. Joannopoulos, and M. Soljačić, Observation of unidirectional backscattering-immune topological electromagnetic states, *Nature (London)* **461**, 772 (2009).
- [4] R. O. Umucalılar and I. Carusotto, Artificial gauge field for photons in coupled cavity arrays, *Phys. Rev. A* **84**, 043804 (2011).
- [5] M. Hafezi, E. A. Demler, M. D. Lukin, and J. M. Taylor, Robust optical delay lines with topological protection, *Nat. Phys.* **7**, 907 (2011).
- [6] K. Fang, Z. Yu, and S. Fan, Realizing effective magnetic field for photons by controlling the phase of dynamic modulation, *Nat. Photonics* **6**, 782 (2012).
- [7] M. Rechtsman, J. M. Zeuner, Y. Plotnik, Y. Lumer, D. Podolsky, F. Dreisow, S. Nolte, M. Segev, and A. Szameit, Photonic Floquet topological insulators, *Nature (London)* **496**, 196 (2013).
- [8] M. Hafezi, S. Mittal, J. Fan, A. Migdall, and J. M. Taylor, Imaging topological edge states in silicon photonics, *Nat. Photonics* **7**, 1001 (2013).
- [9] A. B. Khanikaev, S. H. Mousavi, W.-K. Tse, M. Kargarian, A. H. MacDonald, and G. Shvets, Photonic topological insulators, *Nat. Mater.* **12**, 233 (2013).
- [10] X. Cheng, C. Jouvaud, X. Ni, S. H. Mousavi, A. Z. Genack, and A. B. Khanikaev, Robust reconfigurable electromagnetic pathways within a photonic topological insulator, *Nat. Mater.* **15**, 542 (2016).
- [11] L.-H. Wu and X. Hu, Scheme for Achieving a Topological Photonic Crystal by Using Dielectric Material, *Phys. Rev. Lett.* **114**, 223901 (2015).
- [12] F. Gao, Z. Gao, X. Shi, Z. Yang, X. Lin, H. Xu, J. D. Joannopoulos, M. Soljačić, H. Chen, L. Lu, Y. Chong, and B. Zhang, Probing topological protection using a designer surface plasmon structure, *Nat. Commun.* **7**, 11619 (2016).
- [13] D. Xiao, W. Yao, and Q. Niu, Valley-Contrasting Physics in Graphene: Magnetic Moment and Topological Transport, *Phys. Rev. Lett.* **99**, 236809 (2007).
- [14] W. Yao, D. Xiao, and Q. Niu, Valley-dependent optoelectronics from inversion symmetry breaking, *Phys. Rev. B* **77**, 235406 (2008).
- [15] K. F. Mak, K. L. McGill, J. Park, and P. L. McEuen, The valley Hall effect in MoS<sub>2</sub> transistors, *Science* **344**, 1489 (2014).
- [16] R. V. Gorbachev, J. C. W. Song, G. L. Yu, A. V. Kretinin, F. Withers, Y. Cao, A. Mishchenko, I. V. Grigorieva, K. S. Novoselov, L. S. Levitov, and A. K. Geim, Detecting topological currents in graphene superlattices, *Science* **346**, 448 (2014).
- [17] M. Sui, G. Chen, L. Ma, W.-Y. Shan, D. Tian, K. Watanabe, T. Taniguchi, X. Jin, W. Yao, D. Xiao, and Y. Zhang, Gate-tunable topological valley transport in bilayer graphene, *Nat. Phys.* **11**, 1027 (2015).
- [18] Y. Shimazaki, M. Yamamoto, I. V. Borzenets, K. Watanabe, T. Taniguchi, and S. Tarucha, Generation and detection of pure valley current by electrically induced Berry curvature in bilayer graphene, *Nat. Phys.* **11**, 1032 (2015).
- [19] L. Ju, Z. Shi, N. Nair, Y. Lv, C. Jin, J. Velasco Jr., C. Ojeda-Aristizabal, H. A. Bechtel, M. C. Martin, A. Zettl, J. Analytis, and F. Wang, Topological valley transport at bilayer graphene domain walls, *Nature (London)* **520**, 650 (2015).
- [20] C. L. Kane and E. J. Mele, Quantum Spin Hall Effect in Graphene, *Phys. Rev. Lett.* **95**, 226801 (2005).
- [21] T. Ma and G. Shvets, All-Si valley-Hall photonic topological insulator, *New J. Phys.* **18**, 025012 (2016).
- [22] J.-W. Dong, X.-D. Chen, H. Zhu, Y. Wang, and X. Zhang, Valley photonic crystals for control of spin and topology, *Nat. Mater.* **16**, 298 (2017).
- [23] X.-D. Chen, F.-L. Zhao, M. Chen, and J.-W. Dong, Valley-contrasting physics in all-dielectric photonic crystals: Orbital angular momentum and topological propagation, *Phys. Rev. B* **96**, 020202 (2017).
- [24] X.-D. Chen and J.-W. Dong, Valley-protected backscattering suppression in silicon photonic graphene, *arXiv:1602.03352*.
- [25] C. L. Fefferman, J. P. Lee-Thorp, and M. I. Weinstein, Bifurcations of edge states—topologically protected and non-protected—in continuous 2D honeycomb structures, *2D Mater.* **3**, 014008 (2016).

- [26] C. L. Fefferman, J. P. Lee-Thorp, and M. I. Weinstein, Edge states in honeycomb structures, *Ann. PDE* **2**, 12 (2016).
- [27] C. L. Fefferman, J. P. Lee-Thorp, and M. I. Weinstein, Honeycomb Schroedinger operators in the strong binding regime, *Commun. Pure Appl. Math.* (to be published).
- [28] J. Lu, C. Qiu, L. Ye, X. Fan, M. Ke, F. Zhang, and Z. Liu, Observation of topological valley transport of sound in sonic crystals, *Nat. Phys.* **13**, 369 (2017).
- [29] R. S. K. Mong and V. Shivamoggi, Edge states and the bulk-boundary correspondence in Dirac Hamiltonians, *Phys. Rev. B* **83**, 125109 (2011).
- [30] P. Delplace, D. Ullmo, and G. Montambaux, Zak phase and the existence of edge states in graphene, *Phys. Rev. B* **84**, 195452 (2011).
- [31] A. Szameit and S. Nolte, Discrete optics in femtosecond-laser-written photonic structures, *J. Phys. B* **43**, 163001 (2010).
- [32] See Supplemental Material at <http://link.aps.org/supplemental/10.1103/PhysRevLett.120.063902> for two microscope images of the waveguide and four animations showing diffracted light measured at the output facet as a function of the decreasing laser wavelength when different modes are excited in different domain walls.
- [33] O. Peleg, G. Bartal, B. Freedman, O. Manela, M. Segev, and D. N. Christodoulides, Conical Diffraction and Gap Solitons in Honeycomb Photonic Lattices, *Phys. Rev. Lett.* **98**, 103901 (2007).
- [34] O. Bahat-Treidel, O. Peleg, and M. Segev, Symmetry breaking in honeycomb photonic lattices, *Opt. Lett.* **33**, 2251 (2008).
- [35] Y. Plotnik, M. C. Rechtsman, D. Song, M. Heinrich, J. M. Zeuner, S. Nolte, Y. Lumer, N. Malkova, J. Xu, A. Szameit, Z. Chen, and M. Segev, Observation of unconventional edge states in 'photonic graphene', *Nat. Mater.* **13**, 57 (2014).
- [36] S. Stützer, M. Rechtsman, P. Titum, Y. Plotnik, Y. Lumer, J. M. Zeuner, S. Nolte, G. Refael, N. Lindner, M. Segev, and A. Szameit, Experimental realization of a topological Anderson insulator, in *CLEO: 2015*, OSA Technical Digest (Optical Society of America, Washington, DC, 2015), paper FTh3D-2.
- [37] A. Szameit, F. Dreisow, T. Pertsch, S. Nolte, and A. Tünnermann, Control of directional evanescent coupling in fs laser written waveguides, *Opt. Express* **15**, 1579 (2007).
- [38] X. Wu, Y. Meng, J. Tian, Y. Huang, H. Xiang, D. Han, and W. Wen, Direct observation of valley-polarized topological edge states in designer surface plasmon crystals, *Nat. Commun.* **8**, 1304 (2017).